THE USE OF CT ANALYSIS IN REVEALING STRUCTURAL HETEROGENEITY OF FRESHWATER CARBONATE DECORATION AND CONSTRUCTION STONES

A CT-ANALÍZIS ALKALMAZÁSA AZ ÉPÍTŐ- ÉS DÍSZÍTŐKŐKÉNT HASZNÁLT ÉDESVÍZI KARBONÁTOS KŐZETEK SZERKEZETI ELEMZÉSÉBEN •

ALZOUBI, Nour[1*] ID; GULYÁS, Sándor[1] ID & GEIGER, János[1] ID

[1]The University of Szeged, Department of Geology and Palaeontology,
2-6 Egyetem Str. H-6722 Szeged, Hungary

E-mail: nouralzoubi@geo.u-szeged.hu

Abstract

This article presents the findings of a CT analysis conducted on freshwater carbonate rocks found in the Danube-Tisza Interfluve. These rocks are utilized for both construction and decoration purposes in the medieval buildings of the region. The aim of the study was to uncover some petrophysical properties of the rocks deriving from the Csólyospálos quarry. The proportions of the main constituents of the rocks carry significant information about the formation and alteration history of sedimentary rocks. To comprehend and assess the nature of these processes, as well as the resulting spatial variations, it is necessary to gather quantitative data on the distribution of these constituents at both macro- and microscales. The researchers employed an EM-mixture analysis that considered the density differences among the individual constituents to determine the quantitative characteristics of the main components that form the rocks. By setting a threshold value to distinguish macropores (empty spaces) with lower density values from the solid matrix, the percentage of voids was calculated for each CT slice. The distribution of these voids was examined in three dimensions along all possible axial directions (X, Y, Z). Watershed algorithm, and Laplace operator were applying on selected CT slices that corresponded to areas with similar compositional features. This approach helped identify potential flow directions within the rocks. The spatial distribution and orientation of macropores, which could be visualized using CT at a resolution of over 200 microns, provided valuable insights into the paths through which water could enter the carbonate rocks used for construction or decoration. This information is crucial in understanding structural damage caused by frost weathering and dissolution via capillary action once a static-state flow is established. Furthermore, these findings complement the results obtained from laboratory geotechnical measurements.

Kivonat

A cikk a Duna-Tisza közén található édesvízi karbonátos kőzeteken végzett CT-elemzés eredményeit mutatja be. Ezeket a kőzeteket építési és díszítési célokra egyaránt felhasználják a térség középkori épületeinél. A vizsgálat célja a kőzetek bizonyos mérnökgeológiai és petrofizikai tulajdonságainak feltárása volt a csólyospálosi kőfejtőből vett minták alapján. A kőzetek fő alkotóelemeinek arányai jelentős információkat hordoznak az üledékes kőzetek kialakulási és átalakulási történetéről. E folyamatok természetének megértéséhez és értékeléséhez, valamint az ebből eredő térbeli eltérésekhez mennyiségi adatokat kell gyűjteni ezen alkotóelemek eloszlásáról mind makro-, mind mikroszinten. A szerzők a kőzeteket alkotó fő komponensek mennyiségi jellemzőinek meghatározásához egy várakozás-maximalizálás algoritmust alkalmaztak, amely az egyes alkotóelemek közötti sűrűségkülönbségeket vette figyelembe. Egy küszöbérték beállításával, amely megkülönbözteti az alacsonyabb sűrűségértékkel rendelkező makropórusokat (üres tereket) a komponensektől (mátrix és szemcsék), kiszámították a pórusok százalékos arányát minden egyes CT-szeletre. Ezen pórusok eloszlását három dimenzióban vizsgálták az összes lehetséges tengelyirányban (X, Y, Z). A kutatók a Laplace-operátort alkalmazó vízválasztó módszert is alkalmazták a kiválasztott CT-szeleteken, amelyek hasonló összetételi jellemzőkkel rendelkező területeknek feleltek meg. Ez a megközelítés segített azonosítani a kőzeteken belüli lehetséges áramlási irányokat. A makropórusok térbeli eloszlása és orientációja, amelyeket a CT segítségével jobb mint 200 mikron felbontással lehetett láthatóvá tenni, értékes betekintést nyújtott azokba az

---

utakba, amelyeken keresztül a víz bejuthatott az építésre vagy díszítésre használt karbonátos kőzetekbe. Ez az információ döntő fontosságú a fagyos időjárás okozta szerkezeti károsodás és a kapilláris hatáson keresztül történő oldódás megértéséhez, amint az áramlás állandósult állapotba kerül. Továbbá ezek az eredmények kiegészítik a laboratóriumi geotechnikai mérésekből származó eredményeket.

Introduction

The impact of natural resources on human life is considerable. Finding suitable dwellings has been crucial during life journey. As civilization progressed, people use various materials like mud and stone to construct their buildings (Dubravka et al. 2013; Fodor 2013; Kustár & Szarka 2013). Carbonate rocks have potential economic benefits, ranging from their use as a source of high-quality calcium carbonate to their potential use as building materials (Knauer 1994; Balogh 1994). Freshwater carbonate is an important material in the geological record and has been the subject of various creative implementations and developments recently, which distinguished it from other sedimentary rocks (Capezzuoli & Swennen 2017).

Freshwater carbonate rocks have been widely used as construction materials; like building and pathway stones and decorative elements since ancient times as shown in **Fig. 1**. In Hungary, many ruins from the Arpadian age, such as churches and houses were built using carbonate rocks (Dubravka et al. 2013; Fodor 2013; Kustár & Szarka 2013). Local quarries were used to extract rocks for construction purposes, mainly in churches and windmills as shown in **Fig. 1**. Its shallow depth and easy access encouraged residents to work in quarries and use this hard rock in the foundation and walls of their buildings (**Fig. 2/g**) (Molnár & Botz 1996, Dubravka et al. 2013; Fodor 2013; Kustár & Szarka 2013). The freshwater carbonate rock found in Csólyospálos was formed during the late Pleistocene and Holocene in a hypersaline lake between dunes. The freshwater carbonate sequence consists of multiple lithified strata overlain by non-lithified dolomite mud covered by the topsoil (Molnár 1980).

Limestone is commonly used as a construction material that is constantly exposed to various physical, chemical, and biological processes causing changes in its chemical and physical parameters. However, depending on their composition, porosity, and texture, some carbonate rocks, such as porous, soft limestone, are especially prone to physical and chemical weathering caused predominantly by water infiltrating the rock's voids (De Muynck et al. 2010). On one hand, dissolved salts and freeze-thawing degrade the rock's fabric;

on the other hand, the carbonate matrix slowly dissolves through weathering, which leads to increased porosity and ultimately decreased petrophysical properties. Nevertheless, most lime-stone and dolostone types have proven to be durable materials for construction purposes (Ahmed et al. 2021; Balogh 1994; Knauer 1994). In instances where the mentioned freshwater carbonate rocks are used for construction in Hungary, the major cause of carbonate rock weathering is the absorption of groundwater and infiltration of rainwater, leading to both chemical weathering, such as carbonate dissolution and physical weathering due to freeze-thaw processes (Ruedrich et al. 2011, Claes et al. 2016). To ensure the long-term durability of carbonate rocks used for construction and decoration purposes information on their physical parameters such as strength, porosity, water absorption, and corrosion resistance are indispensable (Hoek 2004, Lin & Zhang 2023). These parameters are generally gained through multiple petrophysical laboratory measurements, such as Pore size distributions were assessed using nuclear magnetic resonance (NMR), while pore throat size distributions and capillary pressure curves were determined using mercury intrusion porosimetry (MIP) (Pires et al. 2017) which can provide us with petrophysical information representative of the total sample. However, the structure and spatial heterogeneity of the void spaces being the main mediator of fluid flow leading to structural damages cannot be revealed using these technologies.

The X-ray computer tomography (CT) technique has been utilized in various sedimentology studies, focusing on both clastic sedimentary rocks (Gooya et al. 2016; Abutaha et al. 2021) and carbonate sedimentary rocks (Alzoubi et al. 2022). CT allows for scanning rock samples in three dimensions providing a high-resolution (mm and micrometre-scale) quantitative and qualitative information on the structure (mineral phases, matrix, and voids) (Peng et al. 2012; Sun et al. 2019; Atrash & Velledits 2020). This technique allows researchers to create a digital model that reveals details of the inner structure of the rock, including the rock-forming components (RFC) based on their density differences expressed in Hounsfield units ((HU), see definition later).

Fig. 1.: Medieval church walls and church foundations built of freshwater limestone of the Danube-Tisza Interfluve, Hungary

1/a Church wall of the monastery of Ecser; 1/b Church wall of the reconstructed church on Church Hill, Kiskunfélegyháza; 1/c The Truncated tower of Soltszentimre; 1/d Ruins at Lajosmizse; 1/e The foundation of the church of Nyárszentlőrinc; 1/f The Franciscan church of Kecskemét; 1/g Wall of the castle in Szeged; 1/h The foundation of the church at Csengele- Bogárhát; 1/i The foundation of the church at Lakitelek. Photo credit: Zsolt Veres (https://akovekmeselnek.hu)

1. ábra: A Duna-Tisza közi édesvízi mészkőből épült középkori templomfalak és templomalapok, Magyarország

1/a Az ecseri kolostor templomfala; 1/b A kiskunfélegyházi Templomhegyen lévő felújított templom fala; 1/c Soltszentimre Csonka tornya; 1/d Romok Lajosmizsén; 1/e A nyárszentlőrinci templom alapja; 1/f Kecskeméti ferences templom; 1/g A szegedi vár fala; 1/h A csengele-bogárháti templom alapja; 1/i A lakiteleki templom alapja. Fotók: Veres Zsolt (https://akovekmeselnek.hu)
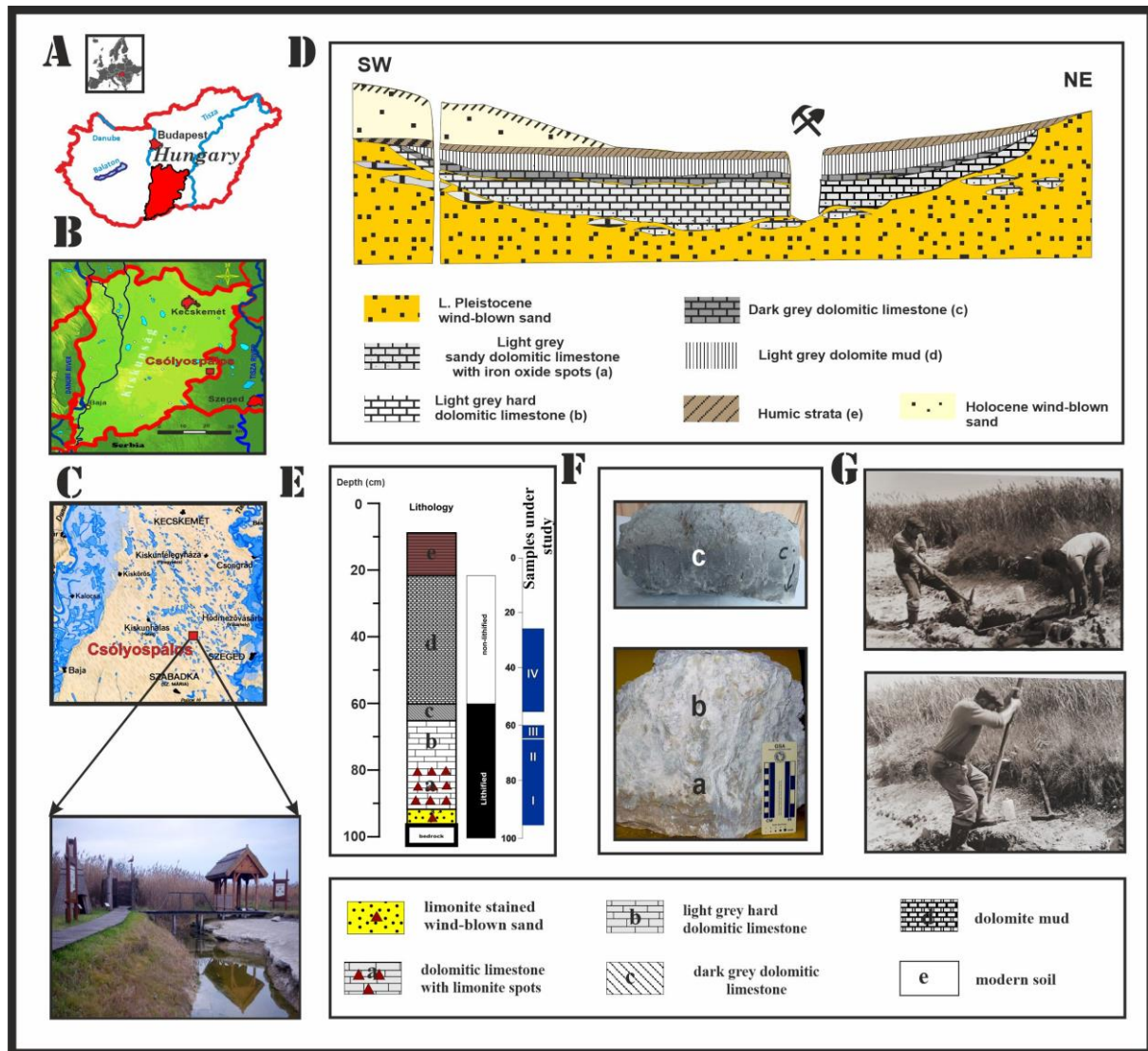
Fig. 2.: Location and stratigraphy of the carbonate sequence studied near Csólyospálos.

A – Map of Hungary. **B** –Location of GHP; **C** – Hydrography of the area, prior to the late 19th century; **D** – Geological cross-section of the site. **E** – Lithology and Schematic log of the outcrop with position of samples under study marked. **F** – Sample -I (Cs1 – Cs2) ab based on Molnár classified, sample II (Cs3) c based on Molnár classified. **G** – digging in the quarry before 1970s.

2. ábra: A Csólyospálos közelében vizsgált karbonátos rétegsor elhelyezkedése és rétegsora.

A - Magyarország térképe. B - A terület elhelyezkedése; C - A terület vízrajza a 19. század vége előtt; D - A terület geológiai metszete. E - A feltárás litológiái oszlopa a vizsgált minták helyzetével. F - I. minta (Cs1 - Cs2) ab a Molnár B. szerinti besorolás alapján, II. minta (Cs3) c a Molnár B. szerinti besorolás alapján. G – kézi fejtés a kőfejtőben az 1970-es évek előtt.

To compare whether carbonate rock is lithified or mud, it is observed that the former exhibits higher HU values. Additionally, variations in HU can arise from changes in sedimentary texture and bulk density (Geiger et al. 2009). Consequently, area with predominantly low density, mainly consisting of voids can be distinguished from regions dominant by high-density matrix. By leveraging CT scans, it is possible to determine the proportions of RFCs based on differences in mineral and particle density (Warlo et al. 2021) caused by processes such as deposition and diagenesis, which involve voids filled with carbonate cement or leaching.

Medical CT scanning can capture voids or empty spaces in materials that are larger than the voxel size (generally greater than 200 microns). Voxel size is calculated by the slice grid resolution (usually 512 × 512 pixels), and the third dimension corresponds to the thickness of the slice (Guan et al. 2019; MRI ACR 2013).

Larger capillary voids which is larger than voxel resolution in this study 200 μm and macropores, are important because they can allow water to infiltrate significant volumes. How these pores are oriented, connected, and shaped determines how deep water can infiltrate into the material, causing structural changes through processes such as chemical

dissolution, salt damage or freezing/thawing cycles (Gireson et al. 2023; Fan et al. 2021). By mapping the distribution, connectivity, and orientation of macropores, and the major direction of PWP within the material, it may be possible to find surfaces and areas that are less prone to infiltration by rain or groundwater and assess the potential water migration paths within the stone itself (Beucher & Meyer 2001).

This inflow will significantly impact on the regions affected by capillary flow within the rock itself. The volume change in the capillary pores during freezing is a major contributor to the rock weathering. However, that capillarity acting against gravity only occurs when the inflowing water is in a static state. So highlighting the distribution of potential water paths(capillary or infiltration paths) can aid in choosing the right orientation of slabs, and tiles and the assignment of areas that may require higher insulation to prevent potential structural changes when the material is used in construction (Pini & Madonna 2016).

Medical CT scanning can capture voids or empty spaces in three dimensions over the scanned materials which reveal the inner details based on the pixel resolution and slice thickness that should be larger than the voxel size (generally greater than 200 microns) to appear in the digital sample.

This study aims to assess the vertical and horizontal spatial variations of void space in selected freshwater limestone samples from the Danube-Tisza Interfluve and assign potential water paths (PWP) thus identifying zones on differently oriented sample surfaces. This inflow will have a significant impact on the regions affected by capillary flow within the sample itself. The orientation and connectivity of macro-voids also influence PWP patterns. Thus, their spatial analysis is essential for the delineation of vertical and horizontal flow paths.

Material and methods

Study area and samples

The Danube-Tisza Interfluve (DTI) is an area of the southern part of central Hungary bounded by the Danube valley to the west, which is a tectonic depression and has an elevation of 90–100 m above sea level (a.s.l). On the other side, it is bordered by the Tisza Valley to the east, which has an elevation of 80 m a.s.l. DTI morphology is formed by an alteration between loess and wind-blown sand (**Fig. 2/d**) (Lóczy 2015). At the end of the Pleistocene and the beginning of the Holocene, many hypersaline lakes formed due to high groundwater levels or surface runoff that accumulated precipitation in the lowest points between dunes. The layers of freshwater limestone

and dolomite mud were as thin as 10–15 cm in some places and as thick as 60–110 cm in others (Jenei et al. 2007; Sümegi et al. 2015; Sümegi & Náfrádi 2015). Samples studied in this research derive from one of the oldest quarries found near the village of Csólyospálos in the south-eastern part of Bács-Kiskun County (**Fig. 2/a,b,c**). The presence of limestone and dolomite mud in Csólyospálos sets it apart from the surrounding area and gives the village cultural and historical significance as one of UNESCO's geological and natural heritage sites, owning both historical and cultural value, especially since limestone quarrying stopped in the 1970s (Dubravka et al. 2013; Fodor 2013; Kustár & Szarka 2013). The geological profile exposing freshwater carbonate layers of 80–110 cm thickness beneath the 15–30 cm topsoil is easily accessible. The freshwater carbonate sequence overlaying the bedrock of the Late Pleistocene wind-blown sand consists of lower lithified carbonate rocks and an upper loose carbonate which is still unlithified carbonate mud (**Fig. 2/e,f**) (Molnár 1991). Freshwater limestone and dolomite mud were utilized as building materials in the surrounding areas (**Fig. 1.**) (Dubravka et al. 2013; Fodor 2013; Kustár & Szarka 2013). Two samples reposited in the sedimentary collection of the Department of Geology and Palaeontology, University of Szeged were subjected to CT scans. Sample I represent members Cs-1 and Cs-2 (between 65 and 90 cm), while sample II represents member Cs-3 (between 60 and 65 cm) (**Fig. 2/f**).

First member Cs-1 is equivalent to Molnár's member A, a 30–40 cm thick dolomitic limestone, stained with iron with a looser structure and vertical veins (**Figs. 2-3.**). This member which has no clear upper boundary transitions to member Cs-2.

Cs-2, equivalent to Molnár's member B is a 40–50 cm thick, light grey, dolomitic limestone with vertical vugs measuring several cm, which correspond to roots of former aquatic vegetation. However, this member called by the locals is *honeycomb stone* due to the visible large voids (**Fig. 1.**). There is a distinct lithological boundary between Cs-2 and the overlying member Cs-3.

Cs-3 equivalent to Molnár's member C, is a very hard, dark-grey dolomitic limestone that is 5–6 cm thick with the highest carbonate content (> 80%) in the entire sequence (**Figs. 2-3.**). This member shows vuggy and moldic porosity, including shelter, gas pores, and desiccation or sheet cracks, in addition to vugs corresponding to roots of former vegetation. Not fully consolidated carbonate mud can be seen formed in some pores. Calcisparite partially or completely infills most of the pores, and pore-filling occurs perpendicularly to the pore wall, forming pore-lining structures (Molnár 1991).
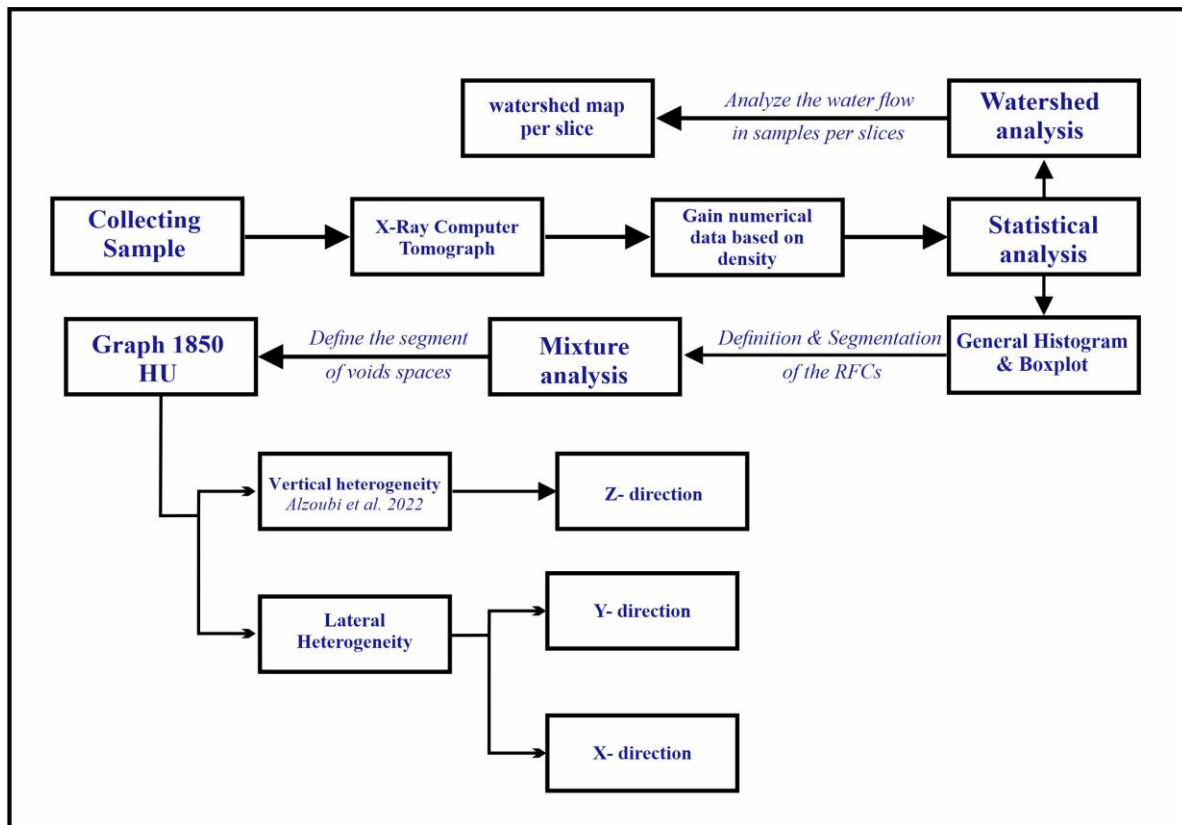
Fig. 3.: The workflow adopted in our work.

3. ábra: Az elemzés lépései

The carbonates in the sample are classified as wackestone and have a mud-supported texture, as figured out by the analysis of thin sections. Matrix (carbonate minerals and detrital material) makes up the majority of RFCs at around 69%, followed by quartz and feldspar grains at about 13.6%, unfilled pores at up to 12%, carbonate lithics at around 3%, and microsite sparite infilling pores at around 2.4%. Tiny amounts of freshwater gastropod shells, calcareous algae oogonia, iron oxides, and manganese minerals are also presented (Molnár & Botz 1996; Molnár et al. 1976; Molnár & Szónoky 1974).

Computer Tomography

Fig. 3. presents the workflow adopted in our work. CT was utilized to generate quantitative three-dimensional data, relying on variation in the density of RFCs expressed by the HU (Hounsfield unit, see below) values. X-ray Computer Tomography (CT) is a modern imaging technique, which works by measuring the attenuation of X-rays as passing through the object under evaluation. Based on signals through a 180° rotation around the object the detectors receive the transmitted X-rays on the opposite side to produce 3D slices (Hounsfield 1973). During an axial movement, a set of 3D slices creates the volumetric data set. It was developed by Hounsfield and Cormack in 1989 and has undergone various resolution improvements and

found applications in non-destructive imaging in fields like geosciences. For instance, CT has been used in palaeontology, clastic rock sedimentology (Földes et al. 2004; Markussen et al. 2019; Abutaha et al. 2021), structural geology to detect faults and fractures (Urbaniec et al. 2018), assess soil porosity (Cnudde et al. 2006), and in engineering (Balázs et al. 2018).

CT images are controlled by various parameters, such as spatial resolution, focal spot size, detector size, crosstalk between detectors, the afterglow of the detectors, and the gantry's rotational speed. A slice image is reconstructed usually by either a filtered back-projection or an iterative reconstruction method, which basically applies Beer Lambert's law (equation 1).

$$I = I_o \cdot e^{-(\mu d)} \qquad (1)$$

where *I* is the intensity of the transmitted X-ray, I_o is the initial X-ray intensity, μ is the linear X-ray attenuation coefficient of the material and d is the length of the X-ray path inside the material along the beam path in the object. By combining slices, a 3D volume is created (Heismann et al. 2003; Duchesne et al. 2009).

A reconstructed slice itself is the map of the linear attenuation coefficient values in that part of the object, which can then be transformed into Hounsfield Units. The Hounsfield unit (HU) is used

to express density differences in the CT image data compared to water's density. HU values are determined using equation 2.

$$HU = 10^3 \cdot [(\mu - \mu_w)/ \mu_w] \qquad (2)$$

where μ is the attenuation coefficient of the material being measured and μ_w is the attenuation coefficient of water. Each HU stands for a 0.1% change in density concerning the calibration density scale. If the measurement is calibrated to distilled water, the resulting HU is 0 for distilled water and 1000 for air.

Visualization and data analysis

The Siemens SOMATOM Emotion 6 medical scanner at the Department of Radiology, University of Pécs, Hungary was used to conduct CT measurements on two samples that represented lithified members of the freshwater carbonate sequence of Csólyospálos (Cs-1, Cs-2, and Cs-3). Sample I corresponds to members Cs-1 and Cs-2 based on (XYZ) order has (130 mm × 45 mm × 480 mm), while Sample II matches member Cs-3 has (240 mm × 180 mm × 100 mm) (as shown in **Figs. 10-11.**). The CT instrument utilized a 140 kVp (peak kilovoltage) setting, with 189 mAs (milliampere-seconds) of current and an exposure time of 1.5 s/image. The lateral resolution was 0.23 mm × 0.23 mm, with a scan-layer thickness of 1.5 mm.

A 3D volume rendering program (Voxler 4.0) was utilized for viewing, filtering, and data extraction from the CT scan files acquired in DICOM format (Digital and Imaging Communications in Medicine). The dataset was filtered by removing the outer portion of the image, resulting in a centrally located CT brick (subset) that is smaller in volume than the original sample (brick of Sample I: in x-y-z order is 101 mm × 31.6 mm× 306 mm; brick of Sample II: 181 mm × 42.3 mm × 42.2 mm). This was done because scanning artifacts like beam hardening can cause the CT value of a single material to change in various parts of an image. There is no cupping shape in the slice profile so there is no considerable bias in the HU values in this volume. Data for the generated CT bricks were used in further statistical analysis.

The RFCs were defined via EM-mixture analysis. This maximum-likelihood non-hierarchical cluster-ing approach is used to find and approximate the parameters (mean and standard deviation) of two or more univariate normal distributions representing overlapping groups corresponding to RFCs relying on the EM-algorithm of Dempster et al. (1977). As this study focuses on spatial distribution and orientation of voids in our brick samples, determining only two major rock-forming components was necessary. Histogram thresholding

is a technique used in image processing to segment an image into different regions based on the intensity values of its pixels.

Histogram thresholding involves selecting a threshold value that separates the image into two or more regions based on the intensity values of the pixels. Pixels with intensity values above the threshold are assigned to one region, while pixels with intensity values below the threshold are assigned to another region. The threshold value can be selected manually or automatically using various algorithms.

Histogram thresholding is a simple and effective technique for image segmentation and is widely used in various applications, such as object detection, image analysis, and pattern recognition. However, its performance can adversely be affected by factors such as noise, illumination, and image quality, and may require further processing techniques to improve its accuracy. After applying EM-mixture analysis of RFCs on the density frequency histogram a most likely threshold value could be defined. The group having the lowest mean HU value, i.e., being the least dense part, was considered as voids, while the remaining groups with higher mean HU values were taken to represent the higher-density components of the matrix. The threshold boundary between the two was found using the logic presented by (Dawson 2011; Coudray et al. 2013). By drawing tangents of the histogram frequency curve at the change in the slope many lines will cross each other which represents the HU value over each crossing point. So, the last cross point with the minimal HU value was chosen as a threshold in this work at ca. 1850 HU. The parts in the frequency distribution represent the density matrix components with higher HU values and the void space at lower HU values. The percentage of RFCs with values less than the mentioned threshold (1850 HU) representing the proportion of the least dense component, i.e., macro voids larger than the resolution of our data (voxel size: 234 μm × 234 μm × 1.5 mm) was determined for each slice and plotted. In addition to gaining, a representative value of the overall RFC composition, the mean HU value per slice was also calculated. Calculations (mean HU value, the cumulative percentage of voids) were performed for individual slices in 3 directions depicted in **Figs. 4-9:** horizontal slices moving from top to bottom along the z-axis, vertical slices moving from left to right along the x-axis, and vertical slices moving from the front to back along the y-axis of the sample brick. This way, we could gain information on the vertical and horizontal heterogeneity of the matrix fabric and the spatial distribution, orientation, and proportion of voids in different samples.
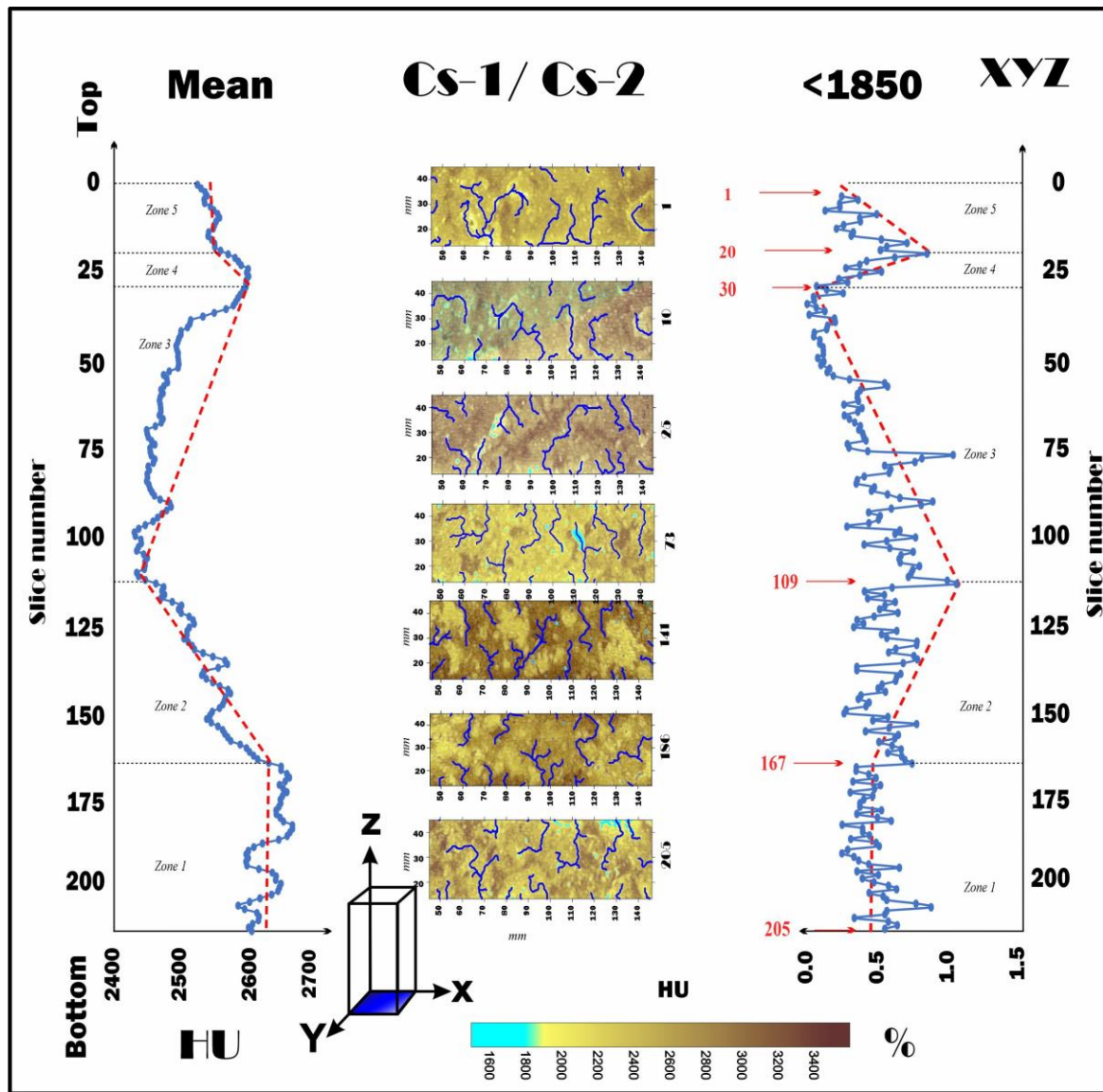
Fig. 4.: Results of analysis done on horizontal slices (x, y) from top (slice 1) to bottom (slice No 205) along the vertical axis (z) of the Sample I brick. (Left graph: variation in mean HU values representing density changes in the sample, right graph: percentages of voids, Centre: horizontal slices characteristic of zones defined based on void percentages, light blue colours show areas of macro voids with HU values below the defined 1850 threshold value, darker shades correspond to the matrix numbers on the slices represent distance in mm)

4. ábra: Az I. minta függőleges tengelye (z) mentén a vízszintes szeleteken (x, y) felülről (1. szelet) lefelé (205. szelet) végzett elemzés eredményei. (Bal oldali grafikon: a minta sűrűségváltozását jelző átlagos HU-értékek változása, jobb oldali grafikon: az üregek százalékos aránya, középen: az üregek százalékos aránya alapján meghatározott zónákra jellemző vízszintes szeletek, a világoskék színek a makroüregek olyan területeit jelzik, amelyek HU-értékei a meghatározott 1850-es küszöbérték alatt vannak, a sötétebb árnyalatok a szeleteken lévő mátrixszámoknak felelnek meg, a szeleteken lévő számok a távolságot jelzik mm-ben.)

The latter also determines the position, length, and orientation of potential water paths (PWP), which serve routes for water entering the sample. To highlight these for selected slices we adopted the method of watershed analysis.

Watershed transformation refers to a geo-morphological watershed, or drainage divide, which separates adjacent drainage basins. Intuitively, a drop of water falling on a topographic relief flow towards the nearest minimum. The nearest minimum is that one at the end of the steepest descent path. In terms of topography, this occurs if the point lies in the catchment basin of that minimum (Beucher & Meyer 1993).

A watershed map reads the data from a grid file and splits the grid up into basin, or catchment areas. The number of basins depends on the areas of the individual basins and is determined by the number of upstream cells that are flowing into the grid cells.
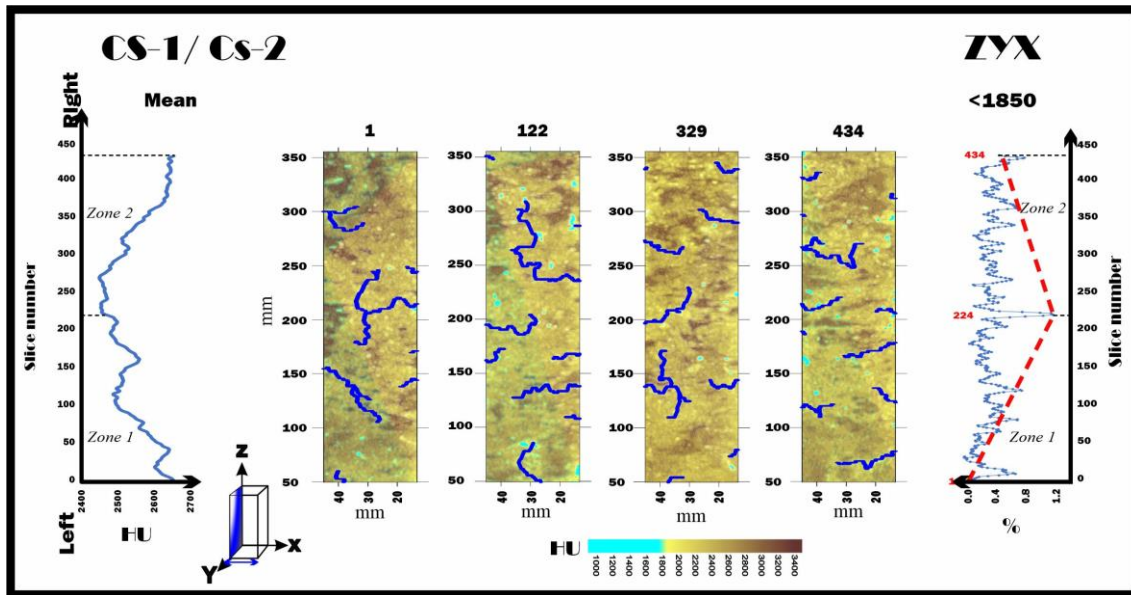
Fig. 5.: Results of analysis done on vertical slices (z, y) from left (slice 0) to right (slice No. 450) along the horizontal axis (x) of the Sample I brick. (Left graph: variation in mean HU values representing density changes in the sample, right graph: percentages of voids, Centre: vertical slices characteristic of zones defined based on void percentages, light blue colours show areas of macro voids with HU values below the defined 1850 threshold value, darker shades correspond to the matrix, numbers on the slices represent distance in mm).

5. ábra: Az I. minta vízszintes tengelye (x) mentén balról (0. szelet) jobbra (450. szelet) a függőleges szeleteken (z, y) végzett elemzés eredményei. (Bal oldali grafikon: a minta sűrűségváltozását jelző átlagos HU-értékek változása, jobb oldali grafikon: az üregek százalékos aránya, középen: az üregek százalékos aránya alapján meghatározott zónákat jellemző függőleges szeletek, a világoskék színek a makroüregek területeit jelzik, amelyek HU-értékei a meghatározott 1850-es küszöbérték alatt vannak, a sötétebb árnyalatok a mátrixnak felelnek meg, a szeleteken lévő számok a távolságot jelzik mm-ben).
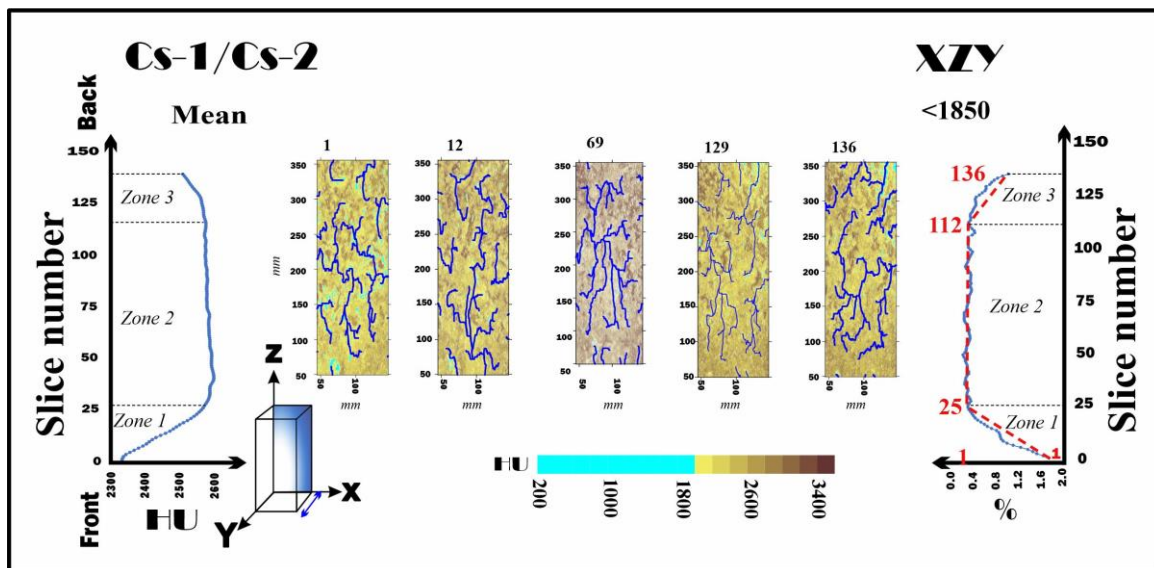

Fig. 6.: Results of analysis done on vertical slices (z, x) from front (slice No. 0) to back (slice No. 150) along the horizontal axis (y) of the Sample I brick. (Left graph: variation in mean HU values representing density changes in the sample, right graph: percentages of voids, Centre: vertical slices characteristic of zones defined based on void percentages, light blue colours show areas of macro voids with HU values below the defined 1850 threshold value, darker shades correspond to the matrix, numbers on the slices represent distance in mm)

6. ábra: Az I. minta vízszintes tengelye (y) mentén az elülső (0. szelet) és a hátsó (150. szelet) függőleges szeleteken (z, x) végzett elemzés eredményei. (Bal oldali grafikon: a minta sűrűségváltozását jelző átlagos HU-értékek változása, jobb oldali grafikon: az üregek százalékos aránya, középen: az üregek százalékos aránya alapján meghatározott zónákra jellemző függőleges szeletek, a világoskék színek a meghatározott 1850-es küszöbérték alatti HU-értékkel rendelkező makroüregek területeit mutatják, a sötétebb árnyalatok a mátrixnak felelnek meg, a szeleteken lévő számok a távolságot jelentik mm-ben).

The larger the threshold value the smaller the number of identified basins is. The calculation of flow lines (flow paths) is based on the amount of flow into the grid node from all surrounding grid nodes. These lines connect the low points on the map. There are several algorithms for watershed transformation (e.g., Beucher & Meyer 1993; Wang & Liu 2006). In this paper, we applied a topological (accurate eight-direction four-point) algorithm using the so-called Laplace operator to assign potential areas of dissipation and confluence, so that non-real potential water paths (PWP) are assigned to the grid at each grid node of the CT slices (Surfer 2023).

Results

Sample I (CS-1 and CS-2 members)

Horizontal heterogeneity

Fig. 4. presents the results of the analysis done on horizontal slices of the first sample (Cs-1 and Cs-2 members) moving in a vertical direction (along the z-axis from bottom to top). The first slice (No. 1) represents the top horizontal part and the last slice (No. 205) the base horizontal part of the brick. This orientation allows us to decipher the horizontal variation in RFCs captured by the mean HU values and those of the voids. The percentage of macro voids (> 200 microns) ranges between 0.05 and 1.24% with an average of approximately 0.56%. Each zone is defined by the bottom and top slice number and represented by an average slice to describe the potential water paths through the zone. From the bottom, the first zone (slices No. 205 to 167) is characterized by high mean HU values (2620–2673) and a relatively smaller proportion of macro voids (0.67–0.39%). In the second zone, there is a gradual increase in macro voids (1.24%) with a peak value in slice No. 109 parallel with decreasing mean HU values down to 2459 HU. In the third zone between slices No. 109 and 30, there is a gradual increase in the density up to 2607 HU alongside decreasing proportions of macro voids to values of 0.11 %. Between slices No. 30–20, we can define zone four which shows slightly increaseing in macro voids percentage up to 0.47% at slice No. 20 with decreasing HU values to 2584. The last zone between the slices No. 20–1 shows a gradual decrease in macro voids percentage to 0.32% with the mean HU density value gradual decrease to (2538 HU).

Fig. 4. also depicts the spatial distribution of macro voids and the density and orientation of water path flow on representative horizontal slices (x, y). The largest percentage of voids is concentrated in the centre of the sample (Zone 2) and the (Zone 4). In Zone 3 below Zone 4 the percentage of large voids is close to zero (0.11%) marking the presence of a good aquitard horizon which could protect the vertical inflow of water to deeper layers even if these voids are communicating. In Zone 1 and Zone 5 the percentage of macro voids is also minimal (0.39% and 0.32%) respectively but not as low as in Zone 3, so here the larger volume of voids may mediate water flow into the sample.

The longest (PWP) is mainly parallel to the y-axis on both sides in all zones. However, the PWP parallel to the x-axis is minimal, as shown in **Fig. 4.** They are generally confined to the left top (slices No. 167, 109, 1) and left central (slice No. 30) part of the slices where macropores appear to be oval-shaped and generally isolated (blue areas in slice No. 109). So, horizontal inflow is generally possible from back to front of the brick in all slices and water can infiltrate as deep as the centre of the sample. It is important to note that flow paths running parallel with the y-axis are less bifurcating, due to their considerable length and density. These potential voids are more likely to keep water in them, and because of changes in the weather temperature, the periodicity of freezing and melting may reduce the efficiency and durability of the stone.

Vertical lateral heterogeneity

The analysis of vertical lateral heterogeneity has been done for both x and y directions. Results of analysis done on vertical slices (z, y) from left (slice No. 1) to right (slice No. 434) along the horizontal axis (x) of the Sample I brick are presented in **Fig.5**. The percentage of macro voids ranged from 0.09 to 1.28%, with an average of approximately 0.44%. Starting from the left side, the first zone, which accounted for almost half of the sample (slices No. 1 to 224), displayed low mean HU values (2653–2469) and a relatively higher proportion of macro voids (0.16–1.26%). Moving further into the sample, the second zone shows a lower percentage of macro voids (0.55%), with an increase in the HU value up to 2655 HU from slice No. 434.

Likewise, to the results of horizontal heterogeneity analysis, PWPs (Potential water paths) are mainly horizontal running parallel with the Y axis of the brick and are concentrated mainly between 100 and 300 mm. However, vertical paths also appear in the central part of the slices where larger pores showing good connectivity and vertical orientation are present (e.g., slice No. 224). Most horizontal PWPs start from the back of the brick.
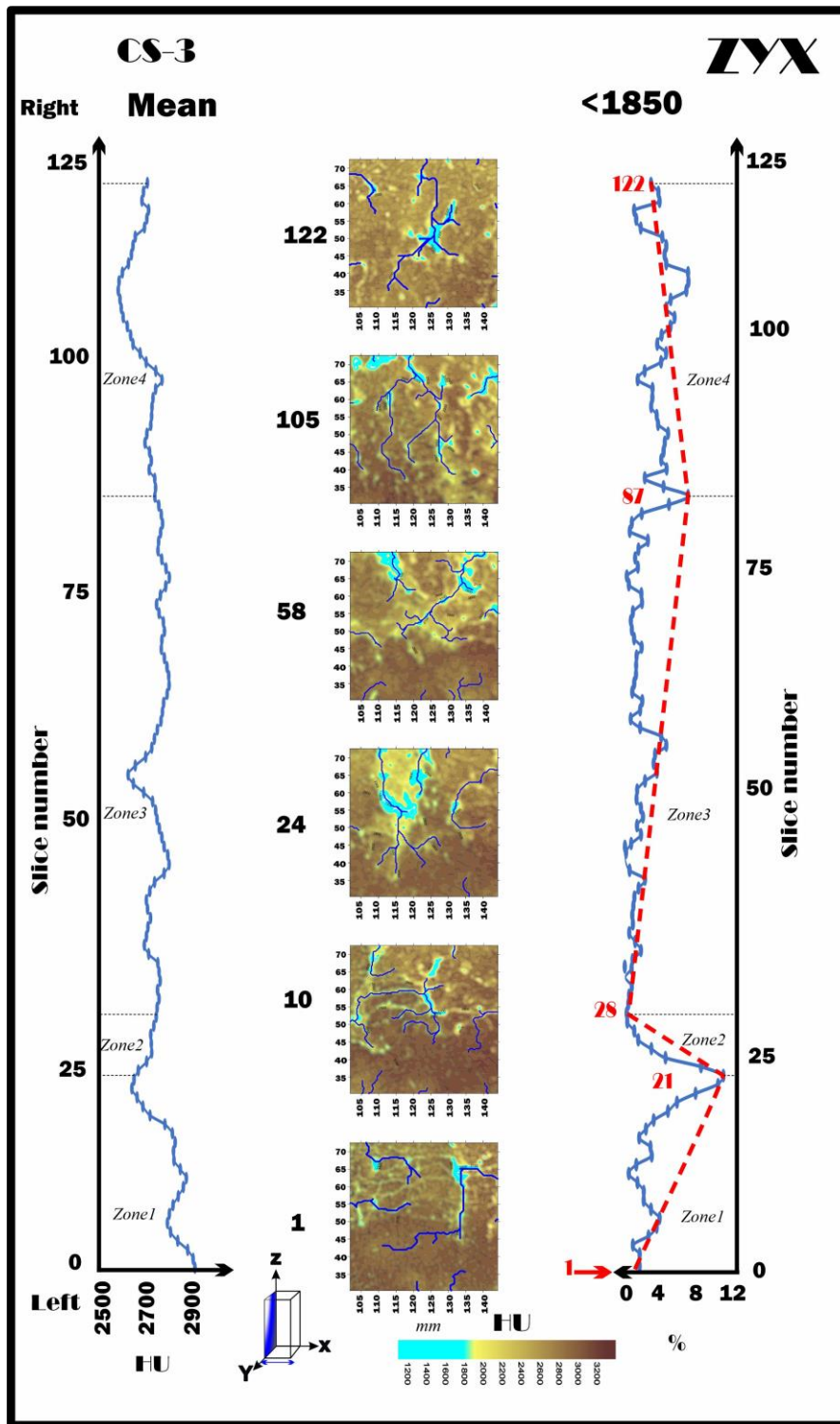
Fig. 7.: Results of analysis done on horizontal slices (x, y) from bottom (slice 0) to top (slice No. 182) along the vertical axis (z) of the Sample II brick. (Left graph: variation in mean HU values representing density changes in the sample, right graph: percentages of voids, center: horizontal slices characteristic of zones defined based on void percentages, light blue colours show areas of macro voids with HU values below the defined 1850 threshold value, darker shades correspond to the matrix, numbers on the slices represent distance in mm)

7. ábra: A II. minta függőleges tengelye (z) mentén alulról (0. szelet) a tetejéig (182. szelet) vízszintes szeleteken (x,y) végzett elemzés eredményei. (Bal oldali grafikon: a minta sűrűségváltozását jelző átlagos HU-értékek változása, jobb oldali grafikon: az üregek százalékos aránya, középen: az üregek százalékos aránya alapján meghatározott zónákra jellemző vízszintes szeletek, a világoskék színek a makroüregek olyan területeit jelzik, amelyek HU-értékei a meghatározott 1850-es küszöbérték alatt vannak, a sötétebb árnyalatok a mátrixnak felelnek meg, a szeleteken lévő számok a távolságot jelzik mm-ben).

Fig. 8.: Results of analysis done on vertical slices (z, y) from left (slice 0) to right (slice No. 122) along the horizontal axis (x) of the Sample II brick. (Left graph: variation in mean HU values representing density changes in the sample, right graph: percentages of voids, Centre: horizontal slices characteristic of zones defined based on void percentages, light blue colours show areas of macro voids with HU values below the defined 1850 threshold value, darker shades correspond to the matrix, numbers on the slices represent distance in mm)

8. ábra: A II. minta vízszintes tengelye (x) mentén balról (0. szelet) a jobbra (122. szelet) függőleges szeleteken (z,y) végzett elemzés eredményei. (Bal oldali grafikon: a minta sűrűségváltozását jelző átlagos HU-értékek változása, jobb oldali grafikon: az üregek százalékos aránya, középen: az üregek százalékos aránya alapján meghatározott zónákra jellemző vízszintes szeletek, a világoskék színek a makroüregek olyan területeit jelzik, amelyek HU-értékei a meghatározott 1850-es küszöbérték alatt vannak, a sötétebb árnyalatok a mátrixnak felelnek meg, a szeleteken lévő számok a távolságot jelzik mm-ben).
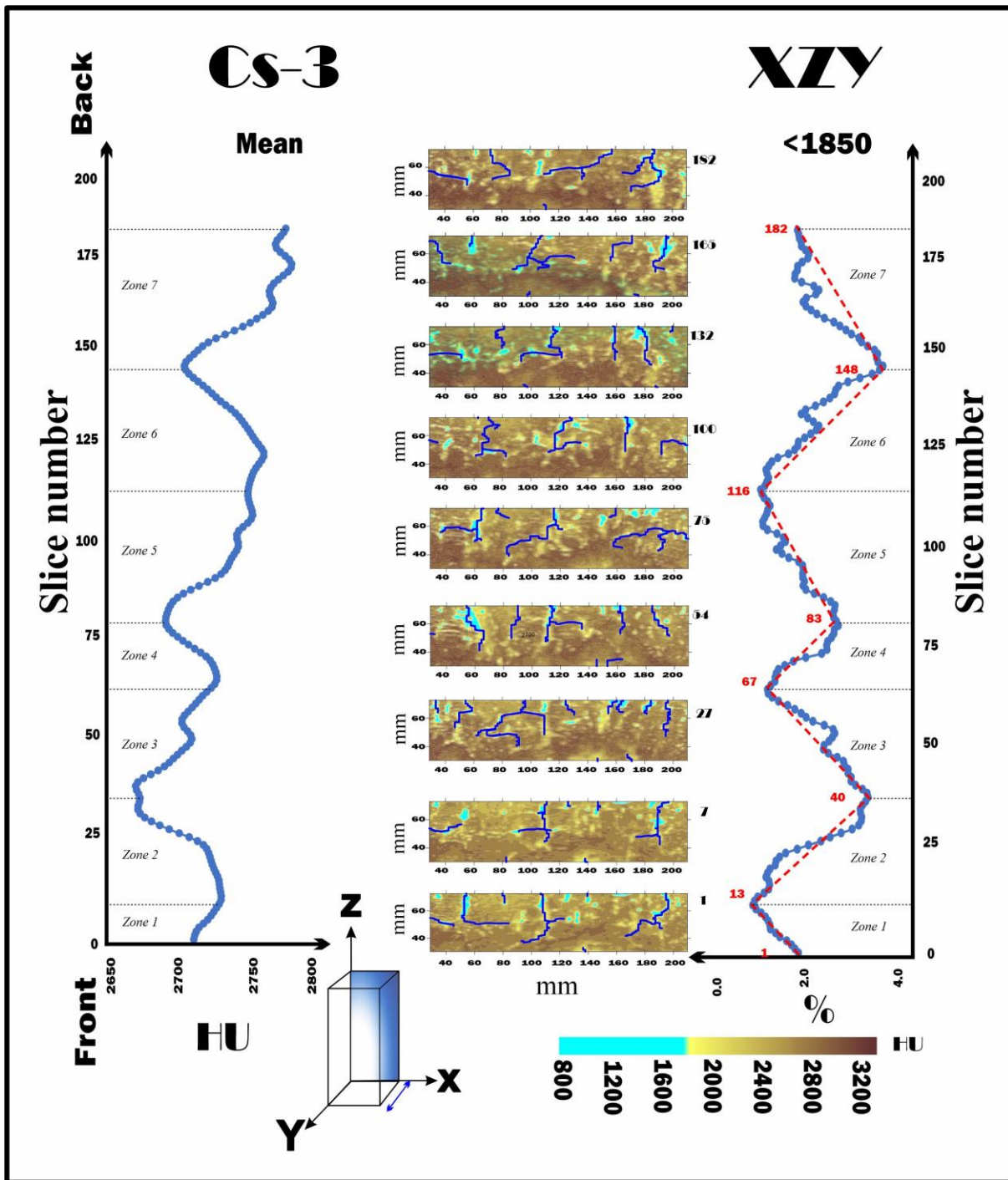
Fig. 9.: Results of analysis done on vertical slices (Z, X) from front (slice No. 1) to back (slice No. 182) along the horizontal axis (y) of the Sample II brick. (Left graph: variation in mean HU values representing density changes in the sample, right graph: percentages of voids, center: vertical slices characteristic of zones defined based on void percentages, light blue colours show areas of macro voids with HU values below the defined 1850 threshold value, darker shades correspond to the matrix, numbers on the slices represent distance in mm)

9. ábra: A II. minta elülső (1. szelet) és hátsó (182. szelet) függőleges szeletein (Z, X) végzett elemzés eredményei a vízszintes tengely (y) mentén. (Bal oldali grafikon: a minta sűrűségváltozását jelző átlagos HU-értékek változása, jobb oldali grafikon: az üregek százalékos aránya, középen: az üregek százalékos aránya alapján meghatározott zónákra jellemző függőleges szeletek, a világoskék színek a makroüregek olyan területeit jelzik, amelyek HU-értékei a meghatározott 1850-es küszöbérték alatt vannak, a sötétebb árnyalatok a mátrixnak felelnek meg, a szeleteken lévő számok a távolságot jelzik mm-ben).

So similarly, to the findings of horizontal heterogeneity analysis if water can enter the brick horizontally from the back or front part of the sample, when reaching the centre where larger vertically oriented pores are present it may continue to a vertical path. After freezing, it again results in

the complete uniform horizontal disintegration of the sample between 100 and 300 mm on the vertical axis (z).

Results of analysis done on vertical slices (z, x) from the front (slice No. 1) to back (slice No. 150) along the horizontal axis (y) of the Sample I brick are presented in **Fig.6**. Here the percentage of macro voids ranged from 0.20 to 1.73%, with an average of approximately 0.44%. Slices could have been divided into three main zones along the y-direction. From slice No. 1 to 25, there is a marked increase in the density from 2332 up to 2563 HU parallelly with a sharp decrease in the total percentage of void spaces from 1.74–0.29%. The next zone between slices No. 25–112 shows a slight increase in density up to 2576 HU and a tiny increase in the percentage of void spaces to values less than 0.003%. The last zone between slices No. 112–136 stands for a sharp decrease in the density down to 2509 HU and a parallel sharp increase in the void's percentage up to 1.02%. So, the largest percentage of voids is confined to the front and back part of the brick (Zones 1 and 3), while the proportion of macro voids is relatively small in the central parts. This is also seen in the density values where zones 1 and three have lower densities and generally higher densities characterize the central part of the brick (Zone 2). So, the proportion of the matrix which gives better physical stability against weathering is higher in the centre. It is also clear that most voids are vertically oriented and show good connections, especially in the central part of the slices between 100 and 300 mm (**Fig. 6**) like the results of the previous vertical heterogeneity analysis (**Fig. 5.**). This holds for all zones.

Sample II (CS-3)

Horizontal heterogeneity

In **Fig. 7.**, the analysis of the second sample (Cs-3 member) was done on horizontal slices which move in a vertical direction along the z-axis from bottom to top. Also here, the first slice (No. 1) represents the base, and the last slice (No. 182) is the top horizontal part of the brick. With this approach, both the voids' and the mean HU values' representations of the horizontal variance in RFCs can be understood. The percentage of macro voids has a range from 0.04 BVS (Below Voxel Size) to 6.60%, with an average of about 2.16%. From the bottom, the first zone is between slices No. 1 and 69, indicated by close to zero macro voids percentage (approximately 0.04% at slice No. 1 displaying a slight increase to the end of the zone to ca. 0.20%). This zone has the highest densities recorded with values between 2845 and 2816 HU. The second zone is between slices No. 69 to 106, characterized by a significant decrease in density down to 2620 HU, alongside the increase in the

proportion of macro voids to values as high as 2.58%. The next zone starts following a break in the trend line right after slice No. 106 showed a sharp increase in macro voids percentage up to 5.41% with a parallel decrease in the density down to 2542 HU. In zone four starting from slice No. 147, the percentage of voids keeps increasing up to 6.60% parallel with decreasing density values down to 2474 HU in slice No. 182.

The sample has a gradual increase in the percentage of voids from the centre to the top (Zone 2, 3, and 4). The fraction of voids in Zone 1 is near zero BVS (0.04%), indicating the presence of a relatively good aquitard horizon that may safeguard the vertical influx of water to the layers above (Zones 2-4). PWPs are relatively short in slice No. 1, run parallel with the y-axis, and are confined in general to the front and back sides of the brick. There is a single path appearing on the left side of Slice No. 1. They have the same orientation and distribution in Slice No. 69, but here PWPs turn longer and new branches running parallel with the x-axis also develop. In addition, the longest PWPs are confined to the front and the proportion of PWPs remains low in the back part of the slice.

As seen in slices No. 1 and 69, despite the low proportion of voids, the horizontal connectivity of the macro voids is good allowing for the infiltration of water from dominantly the front followed by lateral expansion in the upper part of Zone 1. From Zone 2 to Zone 4 despite a steady increase in the proportion and the visible size of macro voids (slice No. 147: bottom right and top left, slice No. 182 bottom left and right) the orientation and length as well as the position of PWPs remain relatively the same as at the boundary of Zone 1. This may be attributed to the relatively considerable number of isolated macropores present in these zones (e. g., slice No. 106: top right, slice No. 182: top left).

Vertical lateral heterogeneity

The analysis of vertical lateral heterogeneity has been done for both x and y directions. Results of analysis done on vertical slices (z, y) from left (slice No. 1) to right (slice No. 122) along the horizontal axis (x) of Sample II brick are presented in **Fig. 8**. Void percentage is between 1% and 4 %. The outlier value of 10% is attributable to the appearance of those two exceptionally large pores which are characterized by large pores by a high diameter ~ 20 mm in **Fig. 8.**, slices No. 21 and 87. Moving from the left side, the first zone of the sample (slice No. 1 to 21) displays low mean HU values (2892–2609) and a relatively higher proportion of macro voids (1.67–10.26%). The second zone shows a sharp decrease in percentage macro voids to 0.34% at slice No. 28 with a slight in the density up to 2708 HU. The third zone, found between slices No. 28 and 87, indicates a clear

increase in the proportion of macro voids up to 7.02% with 2713 HU. Finally, the last zone, found between slices No. 87 and 122, points to a decrease in the proportion of macro voids down to 2.96% with densities decreasing to 2679 HU. Here both the density and the void percentage values remain relatively constant as appeared in **Fig. 8**.

The other minor peaks that were considered correspond to zone boundaries and are interpreted as a sharp increase to 7.02% at slice No. 87 is probably an artifact of the appearance of large pores. So, it seems that void percentage and density remain uniform vertically in the sample, and large increases are attributable to the irregular appearance of exceptionally large macropores. Looking at **Fig. 8.** displaying changes from the front to the back of the brick, it can be seen that vertical PWPs appear systematically and at the same intervals where your peak void % values are noted in this part.

What is visible is that PWPs are longer, more bifurcated, and mainly vertically oriented. They are connected to the exceptionally large macropores in general and their number is relatively small (2–3) which may be attributed to the fact that these large macropores are the mediators of water flow and the remaining pores are mostly isolated as reflected in the low (2–4%) void percentage values in general. It is also worth noting that the largest pores and the most developed PWP are restricted to the left part of the brick (slices No. 1, 21, and 87) and the right (slices No. 1, 28, and 122).

Fig. 9. also supplies the vertical distribution of macro voids along the y-axis from front to back of the brick, the density, and orientation of water path flow on representative horizontal slices (z, x). The percentage of macro voids has ranged from 1.05 to 4.05%, with an average of about 2.34%. Here, seven main zones were interpreted. From the front, the first zone (slices No. 1 to 13) displays a slightly increasing in mean HU values (2696–2713) and a relatively lowest proportion of macro voids by the end of this zone (2.10–1.05%) which indicates in this zone the water will flow down to the centre of the sample and will not infiltrate deeply as shown in **Fig. 9.** slice (No. 1, 13). The Second zone is between slices No. 13 and 40 representing a sharp increase in the proportion of void percentage up to 3.71% and slightly decreasing in the mean density down to 2659 HU. The next one of the longest zones, the third zone, which lies between slices No. 40 and 67, has sharply decreased in the void percentage down to 1.39 % while the mean density increases up to 2710 HU which shows a repeat of the first zone density. The next increasing zone is the second zone shows a high proportion of voids but not high as the second zone here is only up to 3.02% alongside decreasing in the density down to 2678 HU. At slice No. 116 the percentage of voids

decreased to 1.26% parallel to a sharp increase in the HU up to 2731. The sixth zone between slices No. 116 and 148 has the highest peak on the proportion of void percentage up to 4.05% and 2691 HU. The last zone up to the last slice (No. 182) has 2.08 % of the void percentage and the highest density value up to 2754 HU.

Fig. 9. also describes the spatial distribution of macro voids and the density and orientation of water path flow on representative vertical slices (x, z). The largest percentage of voids is concentrated in the top of Zones 2, 4, and 6 with relative percentages of 3.71, 3.02, and 4.05%, respectively. The minimal percentage greater than 1% shows the voids spread over the slice even if there are no connections as appears on slices No. 13, 67, 116, and 182. The longest potential flow (PWP) is mainly parallel to the z-axis, mainly from the top in all zones. However, some isolated short PWP appears from the bottom on slices No. 1, 40, 16, 148 and 182. The PWP parallel to the x-axis is minimal, as shown in **Fig. 9.** only on slices No. 1, 13, and 182 from the left side, and on slices No. 40, 67, and 83 from the right side. Where macropores appear to be oval-shaped and generally isolated. Thus, horizontal inflow is generally possible from left and right, and water can infiltrate as deep as the centre of the sample. It is important to note that flow paths running parallel with the X-axis are less bifurcating, but due to their considerable length and density if water collects in them and freezes it results in a relatively uniform disintegration of the sample.

Discussion and Interpretation

Investigating the void area percentage over the samples in various positions gives information about the surface and inside void spaces in addition to PWPs in various directions. Based on our results of the analysis implemented on vertical and horizontal slices of Sample I the front and the back of the brick appear to be more porous and prone to water uptake by capillary pressure than the left and the right sides of the central part. It is seen in all slices that the length and proportion of PWPs through the left and right directions are negligible on the sides of the brick. So, these lateral parts are less prone to water uptake. Conversely, water may enter the pores from the front, or the back of the brick will be first moving horizontally toward the centre. Once it reaches the interior parts due to the good connectivity and significant percentage of vertically oriented pores flow continues upwards and downwards. Thus, in this example, the front and the back brick position would need either an insulation or a specific orientation during the placement to prevent the inflow of water to the central parts. In the lateral areas, minimal insulation is acceptable, as shown in **Fig. 10**.
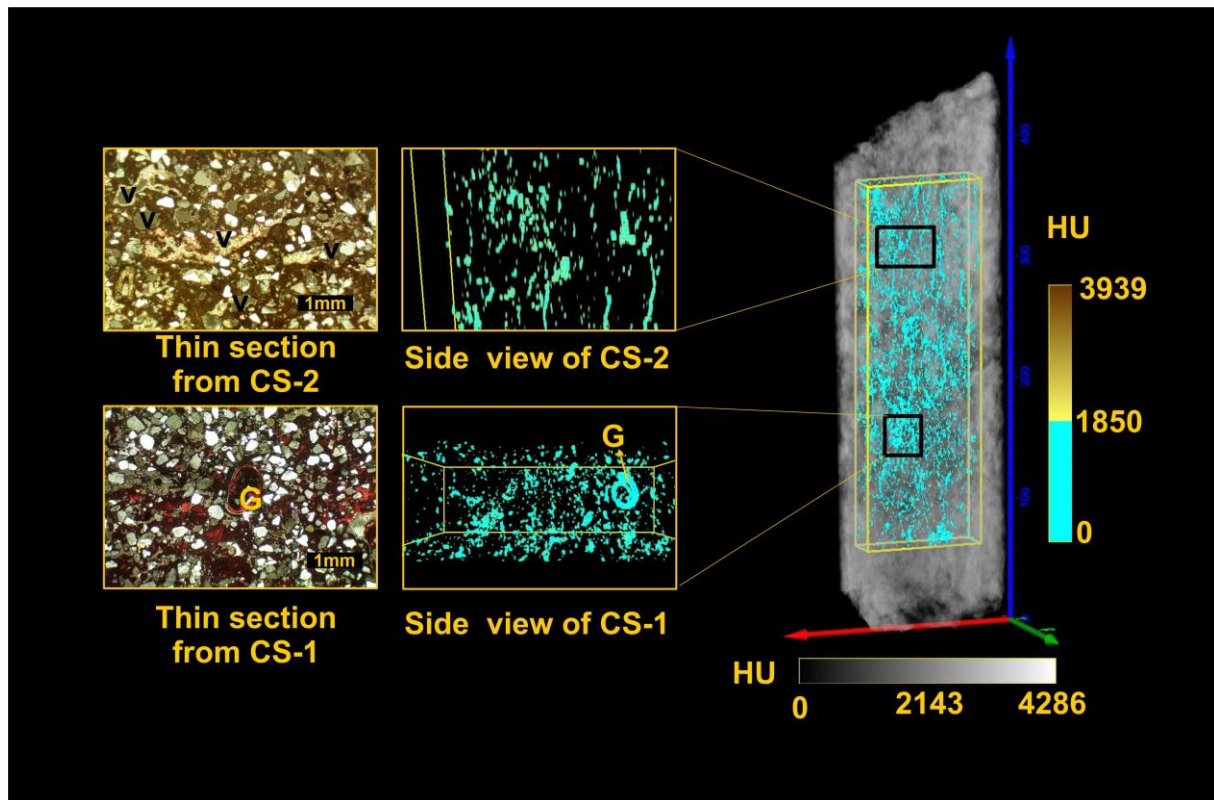
Fig. 10.: 3D void space in Sample I, on the right, is the original sample in greyscale, and the rectangle shows the subset of the sample, the blue shape represents the void space area over the sample's subset in 3D, the black cube shows a side view of void space in Cs-1, the rectangle illustrates the void space in Cs-2, representative thin sections from each member parallel to void space location, V: voids, G: gastropods

10. ábra A jobb oldali I. mintában lévő 3D üres tér az eredeti minta szürkeárnyalatos, és a téglalap a minta részhalmazát mutatja, a kék alakzat a minta részhalmaza feletti űrt jelöli 3D-ben, a fekete kocka oldalnézetben A téglalap a Cs-1 üregterét szemlélteti a Cs-2-ben, reprezentatív vékony szakaszok minden egyes elemtől párhuzamosan az üregtér elhelyezkedésével. V: üregek, G: haslábúak
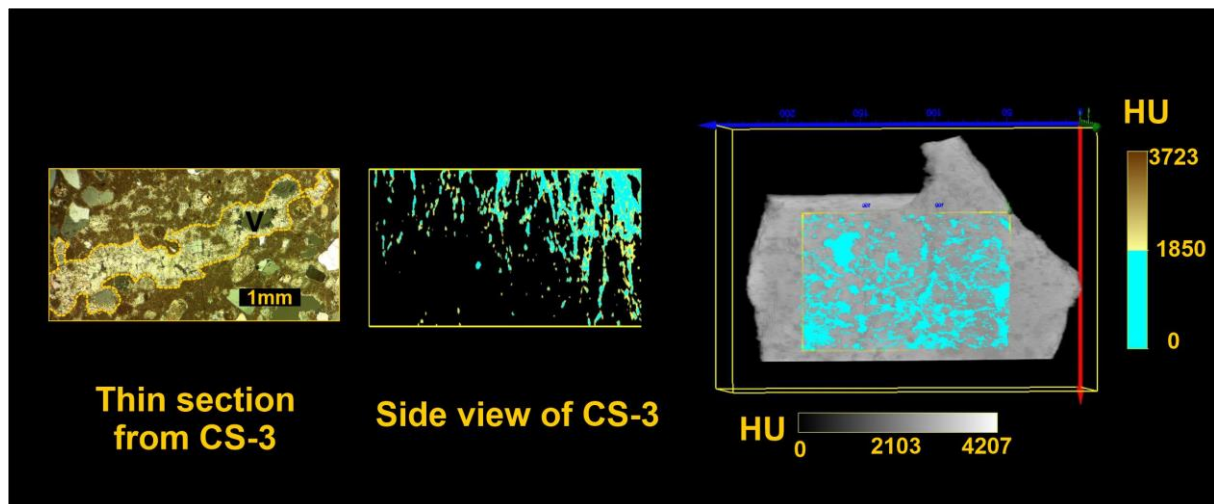

Fig. 11.: 3D void space in Sample II, on the right, is the original sample in greyscale, and the inside rectangle shows the subset of the sample, the blue shape represents the void space area over the sample's subset in 3D, then in the center a side view of void space in Cs-3, on the left side, a representative thin sections from the member parallel to void space location, V: voids.

11. ábra A 3D-s üregtér a II. mintában, a jobb oldalon, az eredeti minta szürkeárnyalatos, a belső téglalap pedig a minta részhalmazát mutatja, a kék alak a minta részhalmaza feletti űrt jelöli 3D-ben, majd az ábra közepén. a Cs-3 üregének oldalnézete, bal oldalon, reprezentatív vékony metszetek az elemtől párhuzamosan az üregek elhelyezkedésével, V: üregek.

The investigation was also carried out on vertical and horizontal slices of Sample II in **Fig. 11**. From the top of the brick appears (in vertical direction) to be more porous and susceptible to water absorption than the horizontal sides. The length and quantity of PWPs on the top of the brick are visible in all slices. As a result, this vertical region is highly susceptible to water absorption. Water possibly will also enter the pores from the front or rear of the brick, moving horizontally toward the centre in the current position of the stone. However, water will enter the bricks less from left or right. Because of the strong connection and high proportion of vertically oriented voids, flow continues downwards once it reaches the internal portions. Consequently, the front and back ends of Sample II would require sufficient insulation to prevent water from entering the inner components. In the lateral portions, only bare essential insulation would be needed.

Conclusion

This research aimed to identify potential weaknesses that may arise from water infiltrating the rock which was used in historical structures and archaeological buildings. However, in turn, helps in determining the cost and points of treatment required for the original stone and its sustainability.

Quantifying voids spaces larger than voxel size (>200 µm) and detecting the potential flow path in freshwater carbonate rock for construction and decoration purposes is fundamental for facilitating and implementing protection for constructed areas. Moreover, it is crucial to forecast these vulnerabilities considering the predicted diurnal variation of temperature, resulting in increased freeze and thaw frequency from severe weather events. To achieve this aim, we used EM-mixture analysis of the CT data to segment RFCs and watershed algorithms to detect the potential of the water flow path.

By showing the spatial distribution and orientation of the potential flow path (PWP) in the watershed map, we can estimate the areas that require enhanced insulation to prevent water inflow and structural damage into the rock. These non-destructive methods provide better insight into the structural heterogeneity of construction stones and complemented by the results of modern petrophysical measurements can supply better models of weathering effects. Furthermore, it helps characterize potential stone materials potentially usable in the conservation of cultural assets.

Generally, the stones varieties which analysed in this study can be regarded as weak stones due to their high open porosity and water absorption capacity paired with low mechanical parameters (Uğur and Toklu 2020, Ruedrich et al. 2011).

The advantages of the method include its non-destructive nature, the ability to obtain visual and quantitative data on rock composition, and the possibility of segmenting rock-forming components (voids and matrix) using statistical approaches. Furthermore, it allows estimation of the percentage of rock-forming components for the entire sample and assessment of spatial variation along the major axes of the studied sample, slice by slice. The method also enables the identification of zones with similar density characteristics and composition, facilitating the evaluation of the distribution, percentage, and orientation of voids within these zones. Additionally, by reconstructing potential water paths, it becomes possible to determine the major direction of flow for each identified zone separately. The 3D visualization of the data enables assessment of the type, orientation, and connectivity of the voids.

This study is limited to using representative samples of the lithified section of freshwater carbonate from Csólyospálos, which probably give precise results if the lithified samples are taken from different points over the dry lake. The results of this work give a preliminary indication of the major direction of voids which are the main potential water paths during water infiltration.

Another limitation of the method is that it is unable to detect micro voids due to their size being smaller than the resolution offered by the medical CT (< 200 microns). Consequently, these micro-voids are not accounted for in the analysis and therefore, the results of this study highlight only a part of the hygric behaviour of the stones. Therefore, to properly detect and understand the hygric behaviour of porous limestones, it is crucial to complete CT measurements with other methods better suitable for measuring the smaller pore sizes.

Contribution of authors

Nour Alzoubi Writing - Original Draft, Visualization, Investigation. **Gulyás Sándor** Conceptualization, Writing - Review & Editing, Supervision. **Geiger János** Writing - Review & Editing, Supervision.

Acknowledgements

References

ABUTAHA, S. GEIGER, J. GULYÁS, S. & FEDOR, F. (2021): Evaluation of 3D Small-Scale Lithological Heterogeneities and Pore Distribution of the Boda Claystone Formation Using X-Ray Computed Tomography Images (CT). *Geologia Croatica* **74/3** 305–318. https://doi:10.4154/gc.2021.17

AHMED, H.G., JAFFAR, H.A. & MURTADHA, J.I. (2021): Petrophysical Study of Limestone Rocks for Al- Nfayil Formation – Bahr Al-Najaf Depression and Suitability for Industrial Purposes. *Journal of the University of Babylon for Pure and applied science* (JUBPAS) **29/1** 75–85. https://journalofbabylon.com/index.php/JUBPAS/article/view/3543/2694

ALZOUBI, N., GEIGER, J. & GULYÁS, S. (2022): Defining rock-forming components of Holocene freshwater carbonates via univariate statistical and mixture analysis of computer tomography data. *Studia Quaternaria* **39/2** 113–128. https://doi:10.24425/sq.2022.140887

ATRASH, H. & VELLEDITS, F. (2020): CT-based analysis of pore network of reservoir rocks. *Geosciences and Engineering* **8/13** 167–184. https://ojs.uni-miskolc.hu/index.php/geosciences/article/view/1824/1214

BALÁZS, Gy., L. LUBLÓY, É. & FÖLDES, T. (2018): Evaluation of Concrete Elements with X-Ray Computed Tomography. *Journal of Materials in Civil Engineering* **30/9** 1–9. https://doi.org/10.1061/(asce)mt.1943-5533.0002389

BALOGH, K. (1994): History of the Hungarian geological survey from 1869 to 1919. In: TÓTH-MAKK, Á. (ed.): *125 years of the history of the Hungarian Geological Survey.* Geological Institute of Hungary, 9–17. http://mek-oszk.uz.ua/18100/18105/18105.pdf

BEUCHER, S. & MEYER, F. (1993): The Morphological Approach to Segmentation: The Watershed Transformation. In: DOUGHERTY, E.R. (ed.): *Advances of Mathematical Morphology in Image Processing*, Marcel Dekker Inc., New York, 433–481.

CAPEZZUOLI, E. & SWENNEN. R. (2017): Non-Marine Carbonates: A Multidisciplinary Approach. *Quaternary International* **437** 1–3. https://doi.org/10.1016/j.quaint.2017.04.005

CLAES, S., SOETE, J., CNUDDE, V. & SWENNEN, R. (2016): A Three-Dimensional Classification for Mathematical Pore Shape Description in Complex Carbonate Reservoir Rocks. *Mathematical Geosciences* **48/6** 619–639. https://doi.org/10.1007/s11004-016-9636-z

CNUDDE, V. MASSCHAELE, B. DIERICK, M. VLASSENBROECK, J. VAN HOO REBEKE, L. & JACOBS, P. (2006): Recent progress in X-ray CT as a geosciences tool. *Applied Geochemistry,* **21/5** 826–832. https://doi.org/10.1016/j.apgeochem.2006.02.010

CORMACK, A.M. & HOUNSFIELD, G.N. (1989): Physiology or medicine 1979: Press release. Accessed April 21, 2018. https://www.nobelprize.org/nobel_prizes/medicine/laureates/1979/press.html

COUDRAY, N. BUESSLER, J. & URBAN, J. (2013): A robust thresholding algorithm for unimodal image histograms. *Pattern Recognition Letters*, **31** 1010-1019. https://doi.org/10.1016/j.patrec.2009.12.025

DE MUYNCK, W., DE BELIE, N. & VERSTRAETE, W. (2010): Microbial Carbonate Precipitation in Construction Materials: A Review. *Ecological Engineering* **36/2** 118–136. https://doi.org/10.1016/j.ecoleng.2009.02.006

DAWSON, R. (2011): How Significant Is a Boxplot Outlier? *Journal of Statistics Education* **19/2**, 1–12. https://doi.org/10.1080/10691898.2011.11889610

DEMPSTER, A.P., LAIRD, N.M. & RUBIN, D.B. (1977): Maximum likelihood from incomplete data via the EM algorithm. *Journal of Royal Statistical Society* **39** 1–38. https://doi.org/10.1115/1.3424485

DUBRAVKA, Đ., STRAŽMEŠTEROV, S. & ĆIRIĆ, L. (2013): A réti mészkő felhasználásának kutatása a Bácska és Bánát északi részén a „CULT-NAT HERIT elnevezésű Magyarország–Szerbia IPA határon átnyúló együttműködési program keretében". In: KUSTÁR, R. & BALÁZS, R. (eds.): A darázskő. Kiskunsági Nemzeti Park Alapítvány, Kecskemét, 131–146.

DUCHESNE, M.J., MOORE, F., LONG, B.F. & LABRIE, J. (2009): A rapid method for converting medical Computed Tomography scanner topogram attenuation scale to Hounsfield Unit scale and to obtain relative density values. *Engineering Geology* **103** 100–105. https://doi.org/10.1016/j.enggeo.2008.06.009

FAN, W., YANG, P. & YANG, Z. (2021): Freeze-Thaw Impact on Macropore Structure of Clay by 3D X-Ray Computed Tomography. *Engineering Geology* **280** (August 2020): 105921. https://doi.org/10.1016/j.enggeo.2020.105921.

FÖLDES, T., ÁRGYELÁN, G.B., BOGNER, P., REPA, I., KISS, B., & HIPS, K. (2004): Application of medical computer tomography

measurements in 3D reservoir characterization. – *Acta Geologica Academiae Scientiarum Hungaricae* **47/1** 63–73.
https://doi.org/10.1556/AGeol.47.2004.1.5

FODOR, G. (2013): "Darázskő szunnyad lejjebb a pagonyban". In: KUSTÁR, R. & BALÁZS, R. (eds.): A darázskő. Kiskunsági Nemzeti Park Alapítvány, Kecskemét, p. 7.

GEIGER, J., HUNYADFALVI, Z. & BOGNER, P. (2009): Analysis of Small-Scale Heterogeneity in Clastic Rocks by Using Computerized X-Ray Tomography (CT). *Engineering Geology* **103/3-4** 112–118.
http://dx.doi.org/10.1016/j.enggeo.2008.06.011

GIRESON, K., ÇELIK, S.B. & ÇOBANOĞLU, İ. (2023): Monitoring the Decrease of Abrasion Resistance on Natural Building Stones Due to Deterioration Caused by Freezing and Thawing Cycles. *Bulletin of Engineering Geology and the Environment* **82/5**, 162–176.
https://doi.org/10.1007/s10064-023-03201-8

GOOYA, R., BRUNS, S., MÜTER, D., MOADDEL, A., HARTI, R.P., STIPP, S.L.S. & SØRENSEN, H.O. (2016): Effect of Tomography Resolution on the Calculated Microscopic Properties of Porous Materials: Comparison of Sandstone and Carbonate Rocks. *Applied Physics Letters* **109/10** 1–5.
http://dx.doi.org/10.1063/1.4962389

GUAN, K.M., NAZAROVA, M., GUO, B., TCHELEPI, H., KOVSCEK, A.R. & CREUX, P. (2019): Effects of Image Resolution on Sandstone Porosity and Permeability as Obtained from X-Ray Microscopy. *Transport in Porous Media* **127/1** 233–245.
https://doi.org/10.1007/s11242-018-1189-9

HEISMANN, B.J. LEPPERT, J. & STIERSTORFER, K. (2003): Density and atomic number measurements with spectral X-ray attenuation method. *Journal of Applied Physics* **94** 2073–2079. http://dx.doi.org/10.1063/1.1586963

HOUNSFIELD, G.N. (1973): Computerized transverse axial scanning (tomography). 1. Description of system. *British Journal of Radiology* **46/552** 1016–1022.
https://doi.org/10.1259/0007-1285-46-552-1016

HOEK, E. (2006): *Practical Rock Engineering.* Evert Hoek Engineering, North Vancouver, British Columbia, 341 p. (accessed September 2023)
https://www.rocscience.com/assets /resources/learning/hoek/Practical-Rock-Engineering-Full-Text.pdf

JENEI, M., GULYÁS, S., SÜMEGI, P. & MOLNÁR, M. (2007): Holocene lacustrine carbonate formation: old ideas in the light of new radiocarbon data from a single site in central Hungary. *Radiocarbon* **49** 1017–1021.
https://doi.org/10.1017/S0033822200042879

KNAUER, J. (1994): Contribution to mineral exploration. 125 years of the history of the Hungarian Geological Survey. In: TÓTH-MAKK, Á. (ed.): *125 years of the history of the Hungarian Geological Survey.* Geological Institute of Hungary, 91–98.
http://mek-oszk.uz.ua/18100/18105/18105.pdf

KUSTÁR, R. & SZARKA, J. (2013): A réti mészkő felhasználása a Duna–Tisza közén. In: KUSTÁR, R. & BALÁZS, R. (eds.): A darázskő. Kiskunsági Nemzeti Park Alapítvány, Kecskemét 87–131.
https://www.knpa.hu/konyvtar/darazsko/

LIN CHAN, C. & ZHANG, M. (2023): Effect of Limestone on Engineering Properties of Alkali-Activated Concrete: A Review. *Construction and Building Materials* **362** (October 2022): 129709.
https://doi.org/10.1016/j.conbuildmat.2022.129709

LÓCZY, D. (2015): Geomorphological Regions. In: LÓCZY, D. (ed.) *Landscapes and Landforms of Hungary*, Springer Cham, Switzerland, 227–235.
https://doi.org/10.1007/978-3-319-08997-3_5

MARKUSSEN, Ø. DYPVIK, H. HAMMER, E. LONG, H. & HAMMER, Ø. (2019): 3D characterization of porosity and authigenic cementation in Triassic Conglomerates/Arenites in the Edvard Grieg field using 3D Micro-CT Imaging. *Marine and Petroleum Geology* **99,** 265–281.
https://doi.org/10.1016/j.marpetgeo.2018.10.015

MOLNÁR, B. (1980): Diagenetic and lithification processes of recent hypersaline dolomites on the Danube-Tisza interfluve. *Mineralogical Magazine* **XXIV/2** 315–337.

MOLNÁR, B. (1991): *Modern lacustrine calcite, dolomite, and magnesite formation in Hungary.* Manuscript, Department of Quaternary Geology, University of Turku, 22 p.

MOLNÁR, B. & BOTZ, R. (1996): Geochemistry and stable isotope ratio of modern carbonate in natron lakes of the Danube-Tisza Interfluve, Hungary. *Acta Geologica Academiae Scientiarum Hungaricae* **39** 153–174.

MOLNÁR, B. & SZÓNOKY, M. (1974): On the origin and geohistorical evolution of the natron lakes of the Bugac Region. *Móra Ferenc Múzeum Évkönyve* **1974** 65–76.

MOLNÁR, B., MURVAI, M.I. & HEGYI-PAKÓ, J. (1976): Recent lacustrine dolomite formation in The Great Hungarian Plain. *Acta Geologica Academai Sociterarum Hungaricae* **20** 179–198.

MRI ACR (2013). MRI Accreditation Program Clinical Image Quality Guide Introduction In: *MRI*

Accreditation Program Clinical Image Quality Guide. American College of Radiology, Reston, Vancouver, 1–38. (MRI Accreditation CIQG 5-22-13.doc)

PENG, S., HU, Q. DULTZ, S. & ZHANG, M. (2012): Using X-Ray Computed Tomography in Pore Structure Characterization for a Berea Sandstone: Resolution Effect. *Journal of Hydrology* **472-473** 254–261.
http://dx.doi.org/10.1016/j.jhydrol.2012.09.034

PINI, R. & MADONNA, C. (2016): Moving across Scales: A Quantitative Assessment of X-Ray CT to Measure the Porosity of Rocks. *Journal of Porous Materials* **23/2** 325–338.
https://doi.org/10.1007/s10934-015-0085-8

PIRES, L.O., FIORELLI, G.L., WINTER, A. & TREVISAN, O.V. (2017): Petrophysical Characterization of Carbonates Heterogeneity. Paper presented at the Offshore Technology Conference Brasil, Rio de Janeiro, Brazil, October 2017. Paper No.: OTC-28098-MS, 936–947.
https://doi.org/10.4043/28098-ms

RUEDRICH, J., KIRCHNER, D. & SIEGESMUND, S. (2011): Physical Weathering of Building Stones Induced by Freeze-Thaw Action: A Laboratory Long-Term Study. *Environmental Earth Sciences* **63(7)** 1573–1586.
https://doi.org/10.1007/s12665-010-0826-6

SUN, H., BELHAJ, H., TAO, G., VEGA, S. & LIU, L. (2019): Rock Properties Evaluation for Carbonate Reservoir Characterization with Multi-Scale Digital Rock Images. *Journal of Petroleum Science and Engineering* **175** 654–664.
https://doi.org/10.1016/j.petrol.2018.12.075

Surfer® (2023) Program and Golden Software. Surfer Quick Start Guide, pp. 61.

SÜMEGI, P., MOLNÁR, D., SÁVAI, S., NÁFRÁDI, K., NOVÁK, Z., SZELEPCSÉNYI, Z. & TÖRŐCSIK, T. (2015): First radiocarbon dated palaeoecological data from the freshwater carbonates of the Danube-Tisza interfluve. *Open Geosciences* **7** 40–52. https://doi.org/10.1515/geo-2015-0003

SÜMEGI, P. & NÁFRÁDI, K. (2015): A radiocarbon-dated cave sequence and the Pleistocene/ Holocene transition in Hungary. *Open Geosciences* **1** 783–798.
https://doi.org/10.1515/geo-2015-0051

UĞUR, İ. & TOKLU, H.Ö. 2020. Effect of Multi-Cycle Freeze-Thaw Tests on the Physico-mechanical and Thermal Properties of Some Highly Porous Natural Stones. *Bulletin of Engineering Geology and the Environment* **79/1** 255–267.
https://doi.org/10.1007/s10064-019-01540-z

URBANIEC, A., DRABIK, K. & DOHNALIK, M. (2018): Selected Features of Carbonate Rocks Based on the X-Ray Computed Tomography Method (CT). *Nafta-Gaz* **74/3** 181–192.
https://doi.org/10.18668/NG.2018.03.01

WANG, L. & LIU, H. (2006): An Efficient Method for Identifying and Filling Surface Depressions in Digital Elevation Models for Hydrologic Analysis and Modelling. *International Journal of Geographical Information Science* **20/2** 193–213.
https://doi.org/10.1080/13658810500433453

WARLO, M. BARK, G. WANHAINEN, CH. BUTCHER, A. FORSBERG, F. LYCKSAM, H. & KUVA, J. (2021): Multi-Scale X-Ray Computed Tomography Analysis to Aid Automated Mineralogy in Ore Geology Research. *Frontiers in Earth Science* **9** 1–24.
https://doi.org/10.3389/feart.2021.789372